Mon. Not. R. Astron. Soc. **000**, 1–15 (2013) Printed 9 January 2014 (MN LATEX style file v2.2)

The star-formation history of mass-selected galaxies from the VIDEO survey

Jonathan T. L. Zwart⋆,[1] Matt J. Jarvis,[1,2] Roger P. Deane,[3] David G. Bonfield,[4] Kenda Knowles,[5] Nikhita Madhanpall,[1,6] Hadi Rahmani[7,8] and Daniel J. B. Smith[4]

[1] *Department of Physics & Astronomy, University of the Western Cape, Private Bag X17, Bellville 7535, South Africa*
[2] *Astrophysics, Department of Physics, Keble Road, Oxford OX1 3RH*
[3] *Astrophysics, Cosmology & Gravity Centre, Astronomy Department, University of Cape Town, Private Bag X3, Rondebosch 7701, South Africa*
[4] *Centre for Astrophysics, Science & Technology Research Institute, University of Hertfordshire, Hatfield, Hertfordshire AL10 9AB*
[5] *Astrophysics and Cosmology Research Unit, School of Mathematical Sciences, University of KwaZulu-Natal, Durban, 4041, South Africa*
[6] *School of Physics, University of the Witwatersrand, 1 Jan Smuts Avenue, Braamfontein, Johannesburg, 2050 South Africa*
[7] *Inter-University Centre for Astronomy and Astrophysics, Post Bag 4, Ganeshkhind, Pune 411 007, India*
[8] *School of Astronomy, Institute for Research in Fundamental Sciences, PO Box 19395–5531, Tehran, Iran*

Accepted —. Received —; in original form 9 January 2014.

ABSTRACT

We measure star-formation rates (SFRs) and specific SFRs (SSFRs) of K_s-selected galaxies from the VIDEO survey by stacking 1.4-GHz Very Large Array data. We split the sample, which spans $0 < z < 3$ and stellar masses $10^{8.0} < M_*/M_\odot < 10^{11.5}$, into elliptical, irregular or starburst galaxies based on their spectral-energy distributions. We find that SSFR falls with stellar mass, in agreement with the 'downsizing' paradigm. We consider the dependence of the SSFR–mass slope on redshift: for our full and elliptical samples the slope flattens, but for the irregular and starburst samples the slope is independent of redshift. The rate of SSFR evolution reduces slightly with stellar mass for ellipticals, but irregulars and starbursts co-evolve across stellar masses.

Our results for SSFR as a function of stellar mass and redshift are in agreement with those derived from other radio-stacking measurements of mass-selected passive and star-forming galaxies, but inconsistent with those generated from semi-analytic models, which tend to underestimate SFRs and SSFRs. There is a need for deeper high-resolution radio surveys such as those from telescopes like the next-generation MeerKAT in order to probe lower masses at earlier times and to permit direct detections, i.e. to study individual galaxies in detail.

Key words: galaxies: evolution – galaxies: high redshift – galaxies: star formation – galaxies: statistics – galaxies: photometry – surveys

1 INTRODUCTION

Untangling the star-formation history of galaxies is of basic importance in validating our knowledge of cosmology via astrophysics; it permits measurement of the build-up of galactic stellar mass, provides constraints on initial conditions, pins down supernova rates and allows us to compare models of chemical evolution (see e.g. Hopkins & Beacom 2006, Kurczynski et al. 2012). The star-formation rate density of the Universe (Madau et al. 1998) is well-constrained to $z \approx 2$ but at higher redshift ($2 < z < 5$) there is still some dispute using different wavelengths. Crucial for calculating the star-formation rate density at higher redshifts, the star-formation rate (SFR) is often determined in one of the following ways (Calzetti 2012, Kennicutt & Evans 2012 and Kurczynski et al. 2012 give excellent reviews):

(i) UV observations (e.g. Lilly et al. 1996, Steidel et al. 1999, Wilson et al. 2002, Feulner et al. 2007, Elbaz et al. 2007, Zheng et al. 2007, Damen et al. 2009, Ellis et al. 2013) reach relatively high redshifts ($z \gtrsim 6$), but are severely obscured by dust, and hence miss a large fraction of the star formation. Emission is from massive, short-lived stars. The SFR is sometimes calculated using e.g. the Bell et al. (2005) relation together with the infra-red luminosity $L_{\rm IR}$, hence $L_{\rm UV+IR}$, or simply directly from the UV (Hilton et al. 2012). UV-derived SFRs have been found to be systematically lower than IR-derived SFRs (see e.g. Hilton et al. 2012

⋆ email: jzwart@uwc.ac.za

and Figure 4 of Burgarella et al. 2013), and UV-derived specific SFRs (SSFRs) show a relative deficit at higher masses compared to radio-derived SSFRs (Pannella et al. 2009; see also below).

(ii) In the rest-frame optical, star-formation rates can be determined from recombination lines such as Hα, Hβ and [OII], with photons emitted by nebulae around young, massive (OB) stars (see e.g. Kennicutt & Kent 1983, Moustakas et al. 2006). However, emission lines must also be corrected for attenuation by dust and variations in excitation, and studies are restricted to low redshifts ($z \lesssim 0.5$) and limited precision, unless use is made of near-infrared spectroscopy (Roseboom et al. 2012, Roseboom et al. 2013). Yet Domínguez Sánchez et al. (2012) find agreement between emission-line indicators and IR indicators (see next point), as well as concluding that metallicity plays an important role.

(iii) Submm/FIR emission is generated from UV photons re-emitted by dust grains in star-formation regions and reveals star formation that is otherwise optically obscured. One can constrain SFRs by estimating $L_{\rm IR}$ (8–1000 μm) via spectral-energy distribution (SED) fitting, then translating that quantity to a SFR via the Kennicutt et al. (1998) relation (e.g. Polletta et al. 2008, Cava et al. 2010). However, extrapolations to higher redshift and/or lower SSFR must be made because (a) relatively poor telescope resolution for single-dish, space-based telescopes such as *Herschel* leads to rapid source confusion and (b) observing from the ground requires excellent weather. There are also two competing systematic effects that tend to under- and over-estimate the SFR respectively: some starlight is *not* absorbed by dust, and evolved stars contribute to dust heating, something that may only be accounted for with full SED modelling (e.g. da Cunha et al. 2012, Smith et al. 2012). In spite of all this, recent results indicate that the cosmic star-formation rate density levels off at $z \approx 3$ then begins to drop at higher redshifts (e.g. Hopkins & Beacom 2006, Lapi et al. 2011, Burgarella et al. 2013, Behroozi et al. 2013).

(iv) Deep radio surveys are able to probe the galaxy SFR because of cosmic-ray and synchroton emission from accelerated electrons in the magnetic fields of supernova remnants (Helou et al. 1985). The relationship between SFR and 1.4-GHz luminosity is calibrated to the far-infrared-radio correlation (e.g. Condon 1992, Haarsma et al. 2000, Yun et al. 2001, Condon et al. 2002, Bell 2003). Radio-wavelength observations are not obscured by dust and their higher angular resolution drastically reduces source confusion, but they may also suffer from AGN contamination (as is the case for all other tracers) and traditionally do not reach deep-enough flux densities to make them useful for studying star formation at high redshift.

(v) X-rays are linked to the SFRs of late-type galaxies because of neutron-star X-ray binaries, and supernova remnants, which therefore couple to young stellar populations having recent star formation, but they may also suffer from AGN contamination. See Norman et al. (2004) and Daddi et al. (2007) for applications of this method. Zinn et al. (2012) have since measured SFRs and SSFRs in stacking *Chandra* data and found much lower rates than in the radio, although the trend of increasing SSFR out to $z = 3$ is at least consistent between the two.

In general, estimates of SFRs from these diverse routes can differ (see e.g. Kurczynski et al. 2012) because of selection criteria, calibrations in the different wavebands, the assumed initial mass function (IMF) and SEDs. By way of an example, SFRs derived from 24-μm fluxes via the infra-red luminosity can be overestimated because of (dominant) contamination by evolved stars (Kennicutt & Evans 2012) or by AGN contamination (see e.g. Martínez-Sansigre et al. 2005, Martínez-Sansigre et al. 2006).

The SSFR is a measure of a galaxy's star-formation efficiency, i.e. the fraction of its mass that could be transformed into stars at a given cosmic time (Dunne et al. 2009). In particular, it informs us about the phenomenon of 'downsizing' (Cowie et al. 1996; Pérez-González et al. 2008), whereby the most massive galaxies have the lowest SSFRs at all redshifts (see e.g. Schiminovich et al. 2007), and so formed their stars earlier and more rapidly than those of lower mass (Rodighiero et al. 2010). In other words, the dominant star-forming population has slowly moved to lower-mass galaxies over cosmic time (Kennicutt & Evans 2012). Although downsizing is widely accepted as the prevailing explanation for the slope of SSFR with stellar mass, a key aim of current and future surveys is to quantify it.

The recent wave of deep near-infra-red surveys, such as the United Kingdom Infrared Deep Sky Survey Ultra-Deep Survey (UKIDSS–UDS; Lawrence et al. 2007) and UltraVISTA (McCracken et al. 2012) are able to constrain stellar mass. The photospheric-emission peak of evolved stars is at roughly 1–2 μm, therefore selection in the $K_{\rm s}$ band is a good approximation to selection by stellar mass (see e.g. Daddi et al. 2007). However, if the SFR is to be calculated from radio emission, counterpart surveys tend to be shallower than in the near infra-red, so it has become commonplace to bin objects statistically (so-called 'stacking'; see e.g. Serjeant et al. 2004, Dole et al. 2006, Ivison et al. 2007, Takagi et al. 2007, White et al. 2007, Papovich et al. 2007, Dunne et al. 2009, Garn & Alexander 2009, Magdis et al. 2010, Bourne et al. 2011, Karim et al. 2011, Heinis et al. 2013, Viero et al. 2013).

Employing stacking in the radio, Dunne et al. (2009) and Karim et al. (2011) selected populations of normal and star-forming galaxies in the K-band using a colour-colour method (BzK) and SED fitting respectively. Dunne et al. (2009) investigated the star-formation history of BzK-selected galaxies from UKIDSS–UDS using stacking of 610-MHz and 1.4-GHz data from the VLA and the Giant Metrewave Telescope (GMRT) respectively. In the analysis of data from the Cosmic Evolution Survey (COSMOS) field, Karim et al. (2011) selected galaxies at 3.6μm, stacking 1.4-GHz VLA data (A and C arrays), with a noise of 8μJy at the centre of their 1.72 deg^2 map. They calculated stellar masses using SED fitting from their photometric-redshift fitting. There was good agreement in SSFR–redshift evolution between these studies, but the dependence of SSFR on stellar mass was found to be much shallower for the UKIDSS data than for COSMOS. Karim et al. (2011) attribute the difference to discrepant stellar-mass estimation methods, rather than to e.g. cosmic variance: Dunne et al. (2009) calculated stellar masses via the absolute K-band magnitude, which might transfer low-mass (where the conversion is less applicable) star-forming galaxies with high SSFRs to higher

masses, causing the SSFR–M_* slope to flatten (Karim et al. 2011).

In this work we present an independent 'stacking' analysis at 1.4 GHz for sources from the VISTA Deep Extragalactic Observations (VIDEO) survey (Jarvis et al. 2013), in order to measure star-formation rates of mass-selected galaxies. The available 10-band photometry allows accurate SED photometric-redshift and stellar-mass estimation, *and* classification of sources into elliptical, irregular and starburst. At the same time, there is an opportunity to test SSFRs determined from semi-analytic models (e.g. Henriques et al. 2012) against observations of a mass-selected sample.

In section 2 we outline the data in hand, going on to describe photometric-redshift and stellar-mass estimation, and the sample selection, in sections 3 and 4. Our stacking method is presented in section 5, and we subsequently describe how we calculate SFRs and SSFRs from radio fluxes/luminosities. Our results and discussion appear in sections 6 and 7 and we conclude in section 8.

We assume radio spectral indices α are such that $S_\nu \propto \nu^\alpha$ for a source of flux density S_ν at frequency ν. All coordinates are epoch J2000. Magnitudes are in the AB system. We assume a ΛCDM 'concordance' cosmology throughout, with $\Omega_\mathrm{m} = 0.27$, $\Omega_\Lambda = 0.73$ and $H_0 = 70\,\mathrm{km\,s^{-1}\,Mpc^{-1}}$ (Komatsu et al. 2011).

2 OBSERVATIONS

2.1 Infrared and Optical Observations

The ongoing VIDEO Survey will eventually cover 12 square degrees over three fields with a view to studying galaxy formation, evolution and clusters. The data presented here, covering $\approx$ 1 square degree, were taken in Z, Y, J, H, and K_s bands. We also use optical data from the overlapping Canada–France–Hawaii Telescope Legacy Survey (CFHTLS–D1; Ilbert et al. 2006) in the u^*, g', r', i', and z' bands. The 5-σ, 2-arcsec-diameter aperture AB-magnitude limits are, as of June 2012, u^*=28.7, g'=28.8, r'=28.4, i'=28.1, z'=27.2, Z=25.7, Y=24.6, J=24.5, H=24.0 and K_s =23.8. Full details can be found in Jarvis et al. (2013).

2.2 Radio Observations

The radio data are described by Bondi et al. (2003), so we give only a summary. The 1.4-GHz Very Large Array (VLA; B-array) observations of Bondi et al. (2003) cover a 1-square-degree field centred on J $2^h\,26^m\,00^s$ $-4^\circ\,30'\,00''$ (i.e. the XMM–LSS field). A mosaic of nine pointings yields a variation in noise of about 20 per cent around 17.5 μJy. The FWHM of the CLEAN restoring beam is 6 arcsec and the map has 2048 $\times$ 2048 1.5-arcsec pixels. CLEAN bias and bandwidth smearing were two issues considered and resolved in the analysis of Bondi et al. (2003). In our stacking analysis confusion from sources below the flux limit may bias our results. However, with a 6 arcsec synthesized beam we use equation 27 from Condon et al. (2012) to estimate the expected source confusion given this beam. We calculate a confusion noise of 0.8 $\mu\mathrm{Jy\,beam^{-1}}$, which is significantly fainter than the signal we measure from the stacking analysis in section 5.

3 SPECTRAL-ENERGY DISTRIBUTIONS

3.1 Photometric-Redshift Estimation

Photometric redshifts were determined using Le Phare (Arnouts et al. 1999, Ilbert et al. 2006, Ilbert et al. 2009). SED templates are taken from Coleman et al. (1980) with a starburst SED due to Kinney et al. (1996), plus a series of SEDs interpolated between all of these and extended with the GISSEL synthetic models from Bruzual & Charlot (2003). Jarvis et al. (2013) provide more details. A histogram of the best-fit photometric redshifts is shown in Figure 1, where we note that our K_s-band selection is sensitive to the older stellar populations.

Bauer et al. (2011) helpfully simulated the effect of using photometric redshifts in the calculation of SFRs and SSFRs, including catastrophic outliers. The assumed photometric redshift uncertainties were gaussian with $\Delta z/(1+z) \approx 0.1$ over the range $1.5 < z < 3$. They found that on average their SFR and SSFR relations were robust even with these uncertainties included, though the uncertainty did increase for less-massive galaxies. To mitigate the effect of uncertain photometric redshifts, we employ relatively large redshift bins compared to the typical photometric uncertainty of $\Delta z/(1+z)$=0.13 for the VIDEO survey (Jarvis et al. 2013). However in section 7.1 we simulate the effects that photometric uncertainties have on our results.

3.2 Stellar-Mass Estimation

With photometric-redshift estimates fixed at the best-fit values found using the SED templates, we fitted GALAXEV templates to each object's photometry using Le Phare in order to obtain an estimate of stellar mass M_* (following Ilbert et al. 2009). We corrected masses obtained from 2-arcsec aperture photometry to total masses using an empirically-derived, redshift-dependent aperture correction.

The templates we considered had three different metallicities ($Z_\odot$ = 0.004, 0.008 and 0.02) and nine different exponentially-decreasing star-formation rates $\propto \mathrm{e}^{-\tau}$, with

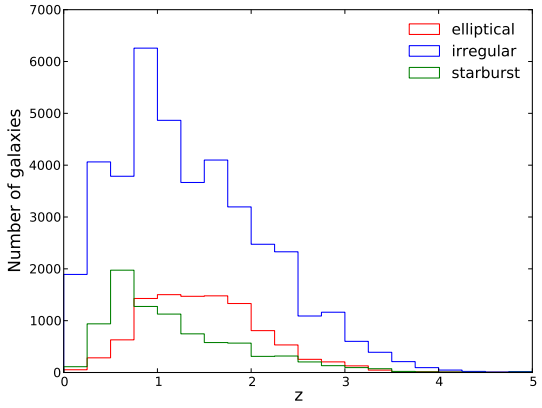

Figure 1. Histogram of best-fit photometric redshifts for each galaxy sample after the data selection described in section 4. Although in this work we only consider sources for which $z < 3$, the histogram shows that there are a number of sources at redshifts $z > 4$.

τ = 0.1, 0.3, 1, 2, 3, 5, 10, 15 and 30 Gyr. We allowed for a dust-extinction correction with $0 < E(B-V) < 0.5$. In each case we assumed a Chabrier initial mass function (Chabrier 2003) and that ages are less than that of the Universe at the corresponding redshift.

The median logarithmic stellar-mass uncertainty for the full sample is $\log_{10}(\Delta M_*/M_\odot) = 0.11$. These uncertainties of course depend on photometric-redshift uncertainties. However, we note that our binning scheme of 0.5 in $\log_{10}(M_*/M_\odot)$ means that this does not influence our results.

4 DATA SELECTION

4.1 Galaxy Classification

We study several different types of population in this work, all selected at K_s band. Galaxies can be classified using a colour-colour diagram (for example, BzK; see e.g. Dunne et al. 2009). However, we classified galaxies based on the best-fitting templates described in section 3.1, in order to investigate the differences between passive and star-forming galaxies. We divided the templates into three sets: ellipticals; Sbc, Scd and irregular galaxies; and starburst galaxies. Template-based classification takes into account the full SED (via 10-band photometry) and ought to be a better discriminator than a colour-colour diagram. Although there may be overlaps, we have split into very broad types using all the available information and as such these types are likely to be robust. We then cut the data in various ways in order to remove contaminants, as detailed in the following sections.

4.2 Star-Galaxy Separation

Following Jarvis et al. (2013), we classify objects as stars if

$$J - K < 0.3 + f_\mathrm{locus}(g-i) \quad (1)$$

where

$$\begin{aligned} f_\mathrm{locus}(x) = &\quad -0.7127 && x < 0.3 \\ f_\mathrm{locus}(x) = &\quad -0.89 + 0.615x - 0.13x^2 \quad \text{for} \quad && 0.3 < x < 2.3 \\ f_\mathrm{locus}(x) = &\quad -0.1632 && x < 2.3, \end{aligned} \quad (2)$$

and where $x = g - i$ and the global offset of 0.1 mag from the Baldry et al. (2010) relation accounts for the difference between K_s and K. We removed all sources that resided in the area of this colour space occupied by stellar sources.

4.3 Further Selection Considerations

Having classified objects by galaxy type, or as stars, we carried out further data selections as follows:

(i) We only consider objects for which K_s <23.5 to ensure that we have a 'complete' sample, since the formal 5-σ limit is 23.8 in K_s band; the completeness of VIDEO at K_s =23.5 was found by Jarvis et al. (2013) to be > 90 per cent.

(ii) We restrict our analysis to objects for which the best-fit redshift $z < 3.0$, since the VIDEO data reach L^* by $z \simeq 3.5$; the VLA data are also insufficiently deep to probe to higher redshifts.

(iii) Some regions of the VIDEO field are contamined by ghosting haloes coming from detector-reflected star light; we therefore excise any K_s-band objects that lie close to the very brightest stars.

(iv) In several cases templates are not (or are poorly) fitted by Le Phare because the data do not sufficiently constrain any model. We only use sources with relatively good photometric-redshift estimates, and therefore impose a template goodness-of-fit $\chi^2 < 50$. This will not bias our results as we only discuss evolutionary trends per source class, and do not tackle the issue of evolution per volume density where such a selection would need to be accounted for.

(v) We remove objects with non-zero SExtractor flags, i.e. those that are too crowded, blended, saturated, truncated or otherwise corrupted.

Of course the fractions removed by each cut depend on the order in which the cuts are applied, and some objects will be multiply-cut; these fractions should therefore only be considered to be approximate: from the original catalogue of K_s-selected objects, 14.0 per cent fail the redshift cut, 3.9 per cent are removed because of haloes, 16.3 per cent have non-zero SExtractor flags and 8.5 per cent have poorly-fitting Le Phare SED templates.

Table 1 summarizes each sample. The final redshift and stellar mass ranges are $0 < z < 3$ and $10^{8.0} < M_*/M_\odot < 10^{11.5}$ respectively. As one moves from elliptical towards starburst galaxies, the median redshift $< z >$ decreases because of the generally lower masses of late types as compared to early types, combined with our K_s magnitude limit.

5 STACKING

The term 'stacking' is vernacular and thus care must be taken over its use. Marsden et al. (2009) defined it as taking the covariance of a map with a catalogue, while other authors use some variation on the technique while at the same time not attempting a definition. *We* take 'stacking' to mean the process of combining data from one set of observations (in this case, the VLA data) using the positions of sources selected from another data set (here, the VIDEO catalogue). The aim is to increase the signal-to-noise ratio for a particular galaxy sample and so describe that population in a statistical way. The combining operation is defined below.

There are many techniques in the literature for stacking data sets (see the examples given in section 1), but two that might be applied here are (i) stacking pixels and assessing the distributions via a mean or median (see e.g. Dunne et al. 2009, Karim et al. 2011), or (ii) modelling the histograms of flux distributions (e.g. Mitchell-Wynne et al. 2013). Here we consider the first, while the second will be presented in a forthcoming paper.

In pixel stacking (see e.g. White et al. 2007), one combines pixel values in the radio-flux map wherever there is a known K_s-selected source (Dunne et al. 2009, Garn & Alexander 2009), to give a distribution of fluxes for that

particular class of object. Since each $K_{\rm s}$-selected source has a corresponding estimate of a photometric redshift and stellar mass, it is further possible to calculate, from these and the radio flux, the radio luminosity of sources as well as the SFRs and SSFRs (see section 6.1). One therefore obtains—for each sample—distributions of fluxes, luminosities, SFRs and SSFRs.

The flux and other distributions are in general non-gaussian and asymmetric because of bright/detected sources and the underlying source-count distribution, so it is not appropriate to simply describe them using a mean and its standard error. On the other hand, a median can, under some circumstances, be subject to its own biases. For example, in their Appendix, Bourne et al. (2012) identify three potential sources of such bias: the flux limits and underlying shape of the 'true' distribution, and the magnitude of the thermal noise. Although Bourne et al. (2012) *did* detect a bias in simulations, it remained small compared to true variations in stacked fluxes, and—crucially—all trends remained significant and conclusions unaffected whether or not a bias correction was applied.

We opt for the median flux (or redshift, luminosity, SFR, stellar mass or SSFR) in this analysis because of its clearly reduced sensitivity to high-flux (or redshift, luminosity, SFR, stellar mass or SSFR) outliers. Note also that because the flux, redshift and stellar-mass distributions are non-gaussian, it is not wise to use their medians to calculate the derived quantities 'directly' (e.g. <SSFR>=<SFR>/<M_*>); instead the full distributions should be used and the medians calculated as the final step. Our adopted error on the median ('median absolute deviation', or MAD), is related to the standard error on the mean σ by $\sigma_{<x>} = \sigma_{\bar{x}}/1.4826$ (Hoaglin et al. 1983). We note, however, that the central-limit theorem does not strictly apply.

During the extraction of fluxes from the radio map, we also excluded regions of the radio map for which the local rms noise is greater than $40\,\mu$Jy, the noise map having been generated following the method of Bondi et al. (2003). In order to test for systematic effects that may have led to non-zero flux in the single-pixel stacks, we repeated our stacking analysis as before, but randomizing the positions of 40,000 sources; that process was then itself repeated to give a total of 300 realisations. The resulting measurement of the median simulated flux was $-0.010 \pm 0.007\,\mu$Jy.

As well as stacking individual pixel fluxes, we have also co-added 41×41 pixel, average flux maps aligned on the positions of the $K_{\rm s}$-selected sources in each sample, in order to provide visual confirmation of our procedure. We compute the weighted-mean *and* median maps and their corresponding standard-error maps. The synthesized beam, below the threshold for CLEANing the 1.4-GHz map, is now evident in both the weighted-mean (Figure 2(a)) and median (Figure 2(c)) maps. Figures 2(b) and 2(d) respectively show the standard-error maps corresponding to the values in the weighted-mean and median maps. Figure 2(b) implies that any uncertainty estimated from a central (i.e. single) pixel will be conservative compared to a method in which the noise is measured, say, far from the centre of the map. We have found that the distribution of pixels in Figure 2(d) is consistent with gaussian noise.

6 RESULTS

6.1 Calculating Specific Star-Formation Rates as a Function of Galaxy Type, Redshift and Stellar Mass

Following Dunne et al. (2009), for each pixel in the radio map where we have a flux $S_{1.4}$ we determined the rest-frame 1.4-GHz luminosity $L_{1.4}$ assuming a spectral index $\alpha = -0.8$. We calculated the SFR by following Condon (1992), Haarsma et al. (2000), Condon et al. (2002) and Dunne et al. (2009):

$$\left(\frac{\rm SFR}{M_\odot {\rm yr}^{-1}}\right) = 1.2006 \times 10^{-21} \left(\frac{L_{1.4}}{\rm WHz^{-1}}\right). \quad (3)$$

The SSFR for each object is then the SFR divided by the stellar mass.

In this analysis we report our results for the dependence of SSFR on stellar mass, as well as for its evolution with redshift.

6.1.1 Separation of SSFR Dependence

In order to quantify the relationship between the SSFR and each of M_* and z, we first note (as do Karim et al. 2011) the assumption suggested by the data that the functional dependence of SSFR on each quantity is separable (uncorrelated), i.e.

$$\mathrm{SSFR}\,(M_*, z) \propto \mathrm{SSFR}\left(M_*|_z\right) \mathrm{SSFR}\left(z|_{M_*}\right) = M_*^\beta (1+z)^n. \quad (4)$$

We therefore fitted these two separate functions of M_* and z using a weighted least-squares estimator:

$$\mathrm{SSFR}\left(M_*|_z\right) = c\,(z)\,M_*^\beta, \quad (5)$$

$$\mathrm{SSFR}\left(z|_{M_*}\right) = C\,(M_*)\,(1+z)^n. \quad (6)$$

In what follows we examine the relationship between SSFR, M_* and z. Note that a typical M_*–z bin contains at least 100 objects.

6.1.2 Dependence on Stellar Mass

In Figures 3(a)–3(d) we show the dependence of SSFR on stellar mass for the different samples: all galaxies, ellipticals,

Table 1. Summary of object samples ($0 < z < 3$). The columns are: (1) Galaxy type; (2) total number of objects in each stack (including 5-σ detections); (3) fraction of sources detected at $> 5\sigma$ in the radio data; and (4) median redshift.

Sample (1)	Number (2)	Detected/% (3)	$< z >$ (4)
all	49604	0.55	1.348
elliptical	9900	1.47	1.442
irregular	33747	0.39	1.334
starburst	5957	0.20	1.207
star	114	0.89	–
millennium	7388770	–	1.250

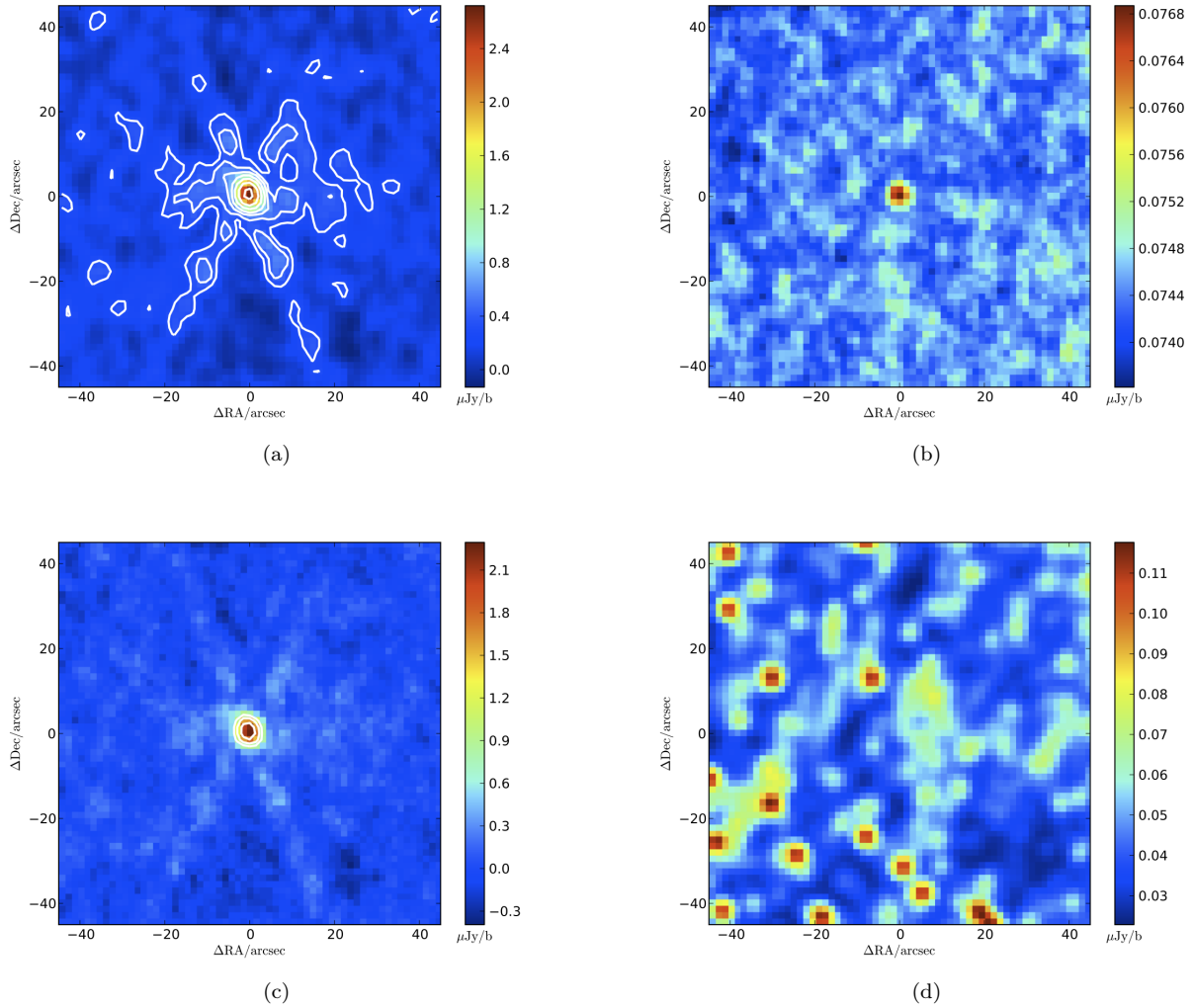

Figure 2. (a) Noise-weighted stacked 1.4-GHz image and (b) its standard-error map. (c) median stacked image and (d) its standard-error map. The uncleaned synthesized beam is evident in (a) and (c). (b) shows how the map noise will be conservative if measured at the central pixel. We have confirmed that the noise structure of (d) is consistent with gaussian noise. Contour levels begin at $\pm 4\sigma$ and increase by a factor of $\sqrt{2}$ thereafter. The 41×41-pixel images have a scale of 1.5 arcsec/pixel.

irregulars and starbursts. As a basic point, we note that SSFRs are significantly higher for the starburst sample than for the other samples. One can also see straightaway the general trend that SSFR decreases with increasing stellar mass.

For the full sample, the 'mass gradient' β_{all} is negative in all cases, but flattens off with redshift (Figure 4(a)), i.e. the steepness of SSFR with stellar mass is lower at higher redshift ($\mathrm{d}\beta/\mathrm{d}z > 0$). We return to this point in section 7. In contrast, for the starburst sample, SSFR is relatively constant with stellar mass (Figure 4(b)). The mass gradient is also shallower for the starburst sample compared to all galaxies, especially at $z \lesssim 1$.

The trend for ellipticals (Figure 5) is almost the same as that for the full sample, confirming that the former population is the dominant contributor to the latter. Just as for β_{sbn}, β_{irr} is less negative than β_{ell} and β_{all}, and roughly independent of redshift, implying that irregular and starburst galaxies are at the same stage of evolution at all redshifts probed. However, for ellipticals, there is evolution, with the low-redshift ellipticals having much lower SSFRs at the high-mass end. In other words, star formation has terminated earlier for ellipticals.

6.1.3 Dependence on Redshift

Figures 6(a)–6(d) indicate how SSFRs for our samples evolve with redshift. One possible definition (used by e.g. Elbaz et al. 2011) of starburst galaxies is those objects for which the SSFR is > 2 times the typical 'main sequence' SSFR. This definition is consistent with our results (Figures 6(a) and 6(d)) that galaxies classified as starbursts from our SED fitting have SSFRs that are greater than approximately a factor of two higher than SSFRs for galaxies in the full sample (see also section 7.3).

Figures 6(c)/6(d) and Figures 6(a)/6(b) show the redshift evolution for irregulars and the starburst sample, and

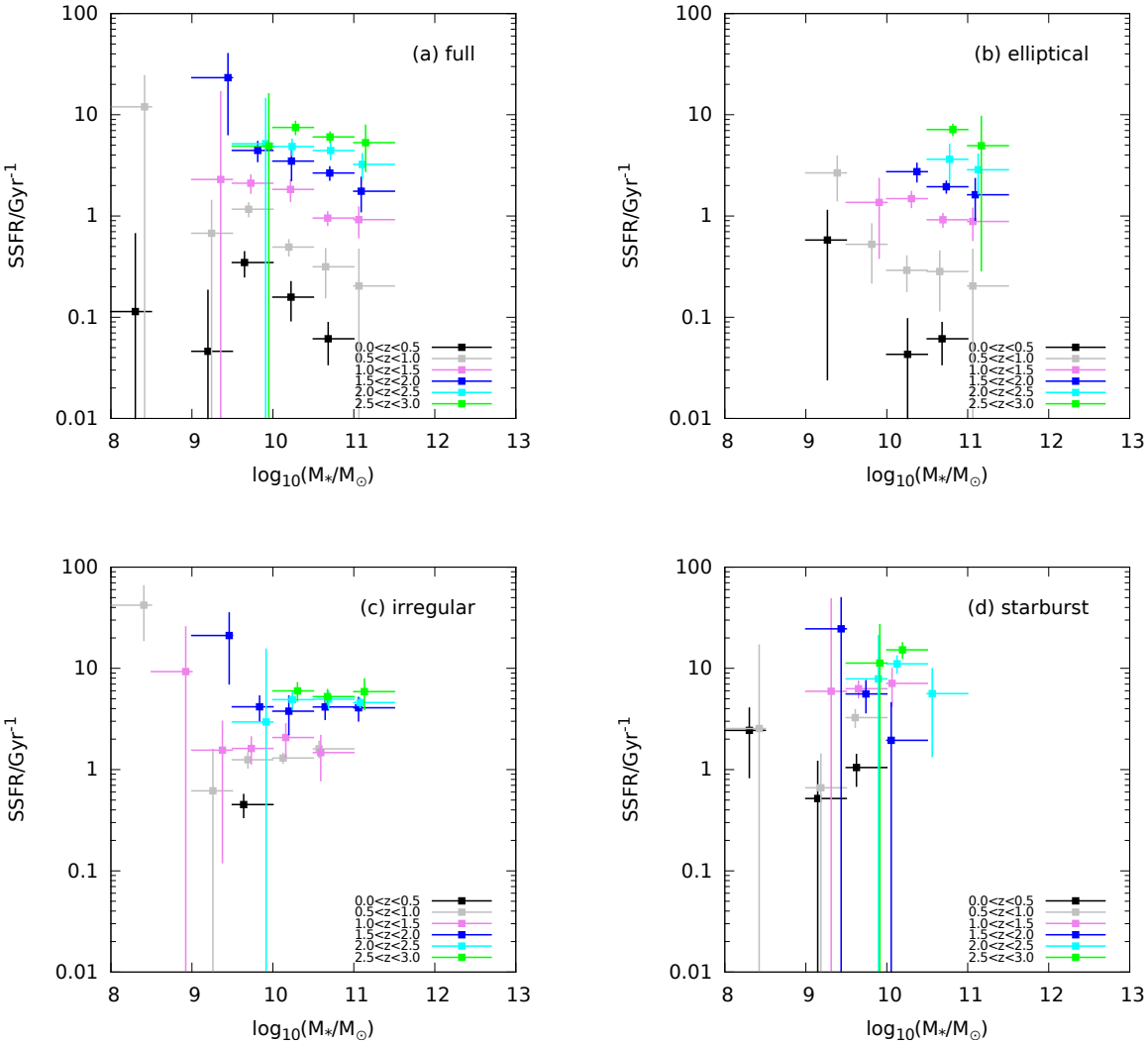

Figure 3. Specific star-formation rate as a function of stellar mass at a given redshift for (a) all galaxies, (b) elliptical galaxies, (c) irregular galaxies and (d) starbursts. SSFR tends to decrease as stellar mass increases, independently of redshift.

for the full sample and the ellipticals, respectively. Compared to the full sample, the gradients for the redshift evolution of the starbursts are shallower (1–5/Gyr^{-1} versus 0.1–5/Gyr^{-1}), i.e. 0.5 decades to 1.4 decades, up to $z \approx 2.5$. This implies that the evolution of the SSFR over cosmic time is much faster for ellipticals than for starburst galaxies, i.e. SSFR in the starburst sample holds up at late times compared to the elliptical sample. We see therefore that more massive galaxies formed their stars earlier than less massive ones, which is consistent with the 'downsizing' scenario (Cowie et al. 1996; Pérez-González et al. 2008). SSFR at a given stellar mass then tends to flatten out by and above $z \approx 2.5$, although our data are limited at higher redshift.

The redshift-evolution parameter n (see Figure 7) is on average higher for all galaxies than for the starburst sample, meaning that, at a given stellar mass, redshift evolution is stronger for the full sample than for the starburst sample. Figure 7 also shows that the redshift evolution n is very distinct for the three different subsamples: the n values for the starburst and irregular samples are consistent with being independent of mass, but the ellipticals exhibit a falling gradient with increasing M_* ($\mathrm{d}n/\mathrm{d}M < 0$). Hence star formation in the highest-mass ellipticals does not evolve as much as for the lowest-mass ellipticals, implying that the morphology as well as mass plays a role in the evolution of the star-formation rate density.

7 COMPARISON WITH SSFRS FROM OTHER ROUTES

In order to set our results in context, we now compare them to those from other work. We have divided the comparison into three subsections: (i) those where K_s-band sources have been stacked at 1.4 GHz, (ii) simulations, and (iii) measurements made using far-infrared SFR indicators. Note that in several cases authors have considered more than one SFR indicator, so a clean separation is not always possible.

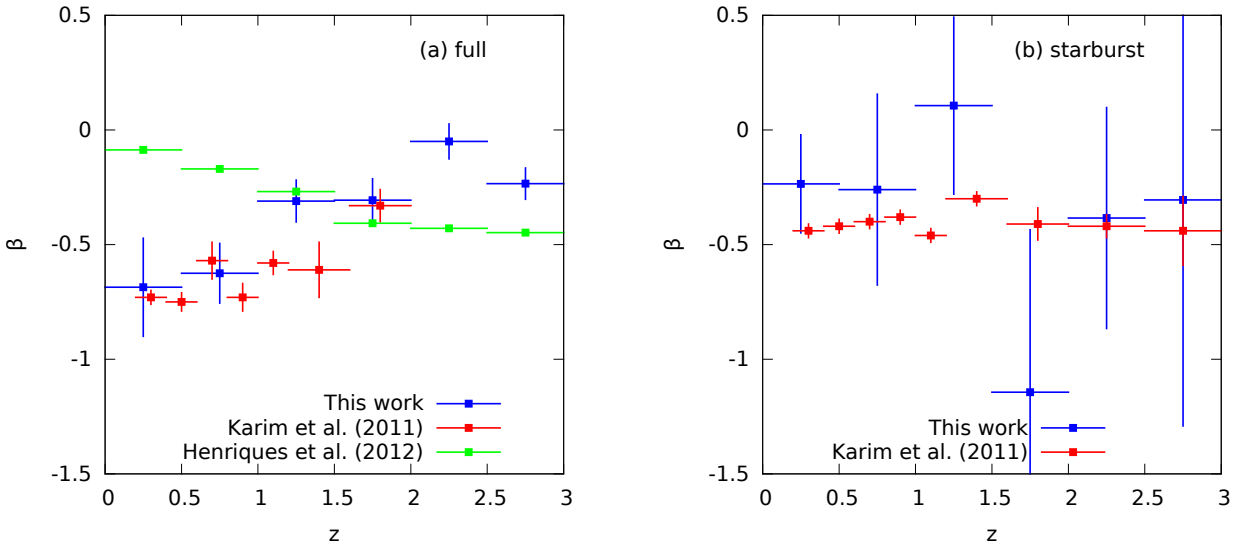

Figure 4. Comparison of mass gradient β of SSFR against stellar mass as a function of redshift for the (a) full and (b) starburst samples.

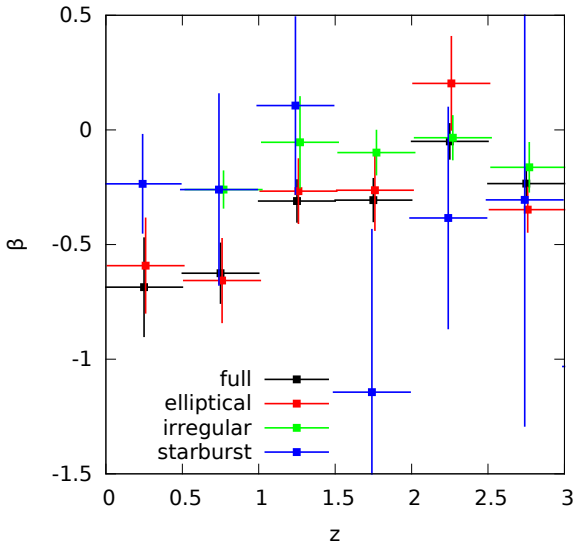

Figure 5. Comparison of gradients β of SSFR as a function of stellar mass at given redshifts for all of our samples.

7.1 SSFRs from Radio Stacking

7.1.1 Dependence on Stellar Mass

We have found that SSFR decreases with stellar mass (downsizing; Figure 3) and increases with redshift (Figure 6), and that the gradients β, though all negative, become shallower with increasing redshift ($\mathrm{d}\beta/\mathrm{d}z > 0$). Our results therefore agree qualitatively with those of Karim et al. (2011), out to $z \approx 2$. Comparing Karim et al. (2011)'s Figure 6 with our Figures 3 and 6, our SSFRs are slightly higher than theirs for the starbust sample, but the dynamic ranges are of the same order for both the starburst sample and for all galaxies.

Quantifying, Figure 4(a) includes a comparison of our measurements of β as a function of redshift for the full sample. Extending the study of Karim et al. (2011) to higher redshift, we find that β continues to flatten with redshift with approximately the same gradient $\mathrm{d}\beta/\mathrm{d}z$ ($\gtrsim 0$).

Figure 4(b) shows $\beta\,(z)$ for the starburst sample; the mass slope β_{sbn} is independent of redshift, with a weighted-mean slope β_{w} of -0.44 ± 0.18), in agreement with the Karim et al. (2011) findings. (Their Table 4 refers; it is not clear whether their 'standard error' is that on the mean or not, but our conclusion is unaffected.) Karim et al. (2011) concluded for a starburst sample that β is independent of redshift, but note, as do Elbaz et al. (2011), that the level and shape of $\beta(z)$, including any potential 'upsizing' (Rodighiero et al. 2010, Oliver et al. 2010), is a strong function of how such starburst objects are selected: negative for a mildly star-forming population but 'flat' (i.e. $\mathrm{d}\beta/\mathrm{d}z = 0$) for actively star-forming galaxies. Karim et al. (2011) only use 21 SEDs (to our 62) in determining redshifts and stellar masses, with an additional colour-colour cut. We therefore advocate that our results for the mass slopes are consistent with those of Karim et al. (2011), but our data do not permit us to investigate the upsizing scenario (i.e. that β steepens with z at $z \gtrsim 3$) seen by Rodighiero et al. (2010) and Oliver et al. (2010).

The SSFRs measured by Dunne et al. (2009), derived using the Condon calibration, are higher than ours for the star-forming galaxies, which emphasizes the different selection functions and methodologies. For example, we use the complete SEDs to estimate stellar masses, whereas Dunne et al. (2009) use only the K-band absolute magnitude. They find that SSFR increases strongly with redshift, for all galaxies and all stellar-mass bins, except that the SSFRs in the higher-mass bins flatten off at early times. This 'bimodality' in the SSFR-M_* plane, with excess 'red and dead' galaxies at higher stellar masses (in other words, extrapolation to lower stellar masses generally overpredicting SSFRs), is also seen by Karim et al. (2011), but is only hinted at in our data in the lowest two redshift bins. Dunne et al. (2009) further found that SSFR decreases slowly with stellar mass, and

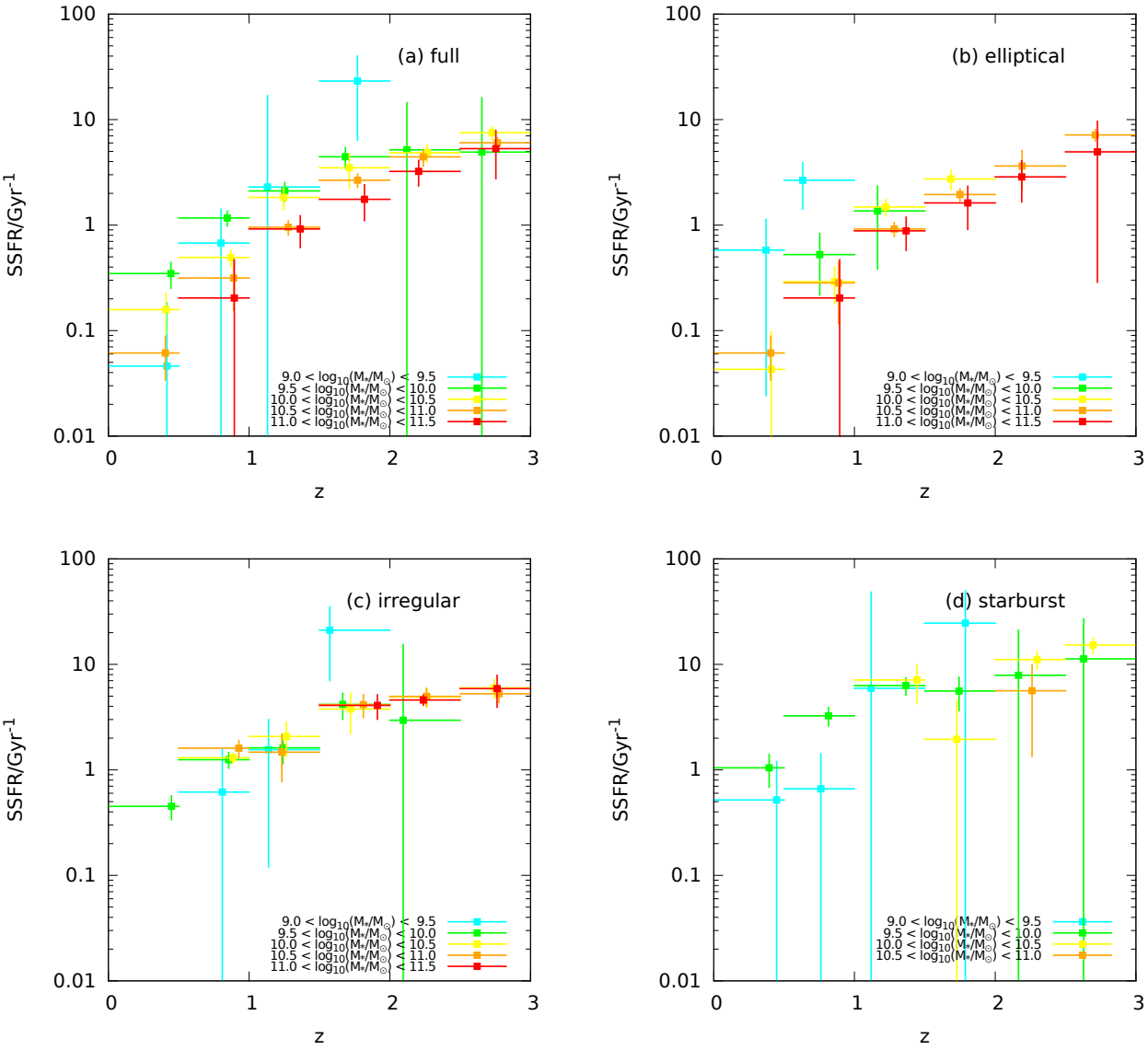

Figure 6. Specific star-formation rate as a function of redshift at a given stellar mass for (a) all galaxies, (b) ellipticals, (c) irregular galaxies and (d) starburst galaxies. SSFR increases with redshift.

that the stellar-mass slope β_{all} *steepens* with z ($\mathrm{d}\beta/\mathrm{d}z < 0$); this is in contrast to our findings and those of Karim et al. (2011). As noted above and in section 1, this is almost certainly due to the way in which the Dunne et al. (2009) stellar masses have been estimated.

Dunne et al. (2009) find that SSFR as a function of cosmic time for their sBzK sample evolves less than for a non-BzK sample. We find the same if we equate our starburst sample with their sBzK, and our full sample with their non-BzK sample. The fact that the stellar-mass estimation by Dunne et al. (2009) is via the rest-frame K-band absolute magnitude (cf. Serjeant et al. 2008), rather than by the SED-fitting method shared by our work and that of Karim et al. (2011), is the sole major methodical difference that might explain the apparent discrepancy. Dunne et al. (2009) note the potential introduction of systematics by their SFR–M_* conversion method and warn against overinterpretation.

Rather than using SED fitting, Pannella et al. (2009) selected star-forming sBzK galaxies at $z \approx 2$, deriving SFRs from stacked VLA 1.4-GHz data over the COSMOS field and paying particular attention to cleaning AGN from their sample. Pannella et al. (2009) find the slope β_{sBzK} is zero (flat) at $z \approx 2$ from 1.4-GHz data, but negative in the UV, i.e. more massive galaxies have SEDs that may be subject to greater extinction. This highlights the problem of dust attenuation for UV star-formation tracers, and so, as expected, our results at $z \approx 2$ are consistent with their radio-stacking results but inconsistent with their UV index, although it may be possible to reconcile the two by including the effects of extinction.

In section 3.1 we asserted that our results would not be biased by neglecting the typical photometric-redshift uncertainties of $\Delta z/(1+z)$=0.13. In order to test this statement, we re-analyzed the full-sample data with gaussian un-

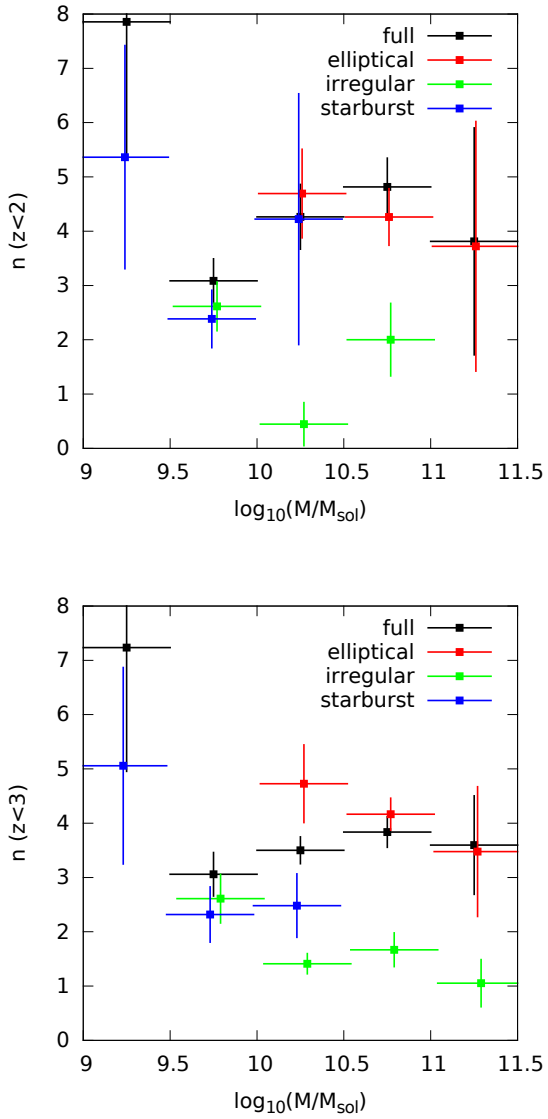

Figure 7. Comparison of redshift-evolution parameters n of SSFR as a function of stellar mass for all of our samples. **Upper panel:** $0 < z < 2$ and **Lower panel:** $0 < z < 3$.

certainties (i.e. Δz=0.13$(1 + z)$) introduced to the original photometric-redshift estimates. We also re-analyzed those data with gaussian uncertainties additionally introduced to the original stellar-mass estimates ($\log_{10}(\Delta M_*/M_\odot) = 0.1$). We found no discernable differences in either the values of β nor in the shape of $\beta(z)$ (Figure 8).

In summary, we find good agreement among the different radio-derived SSFRs, as a function of stellar mass, from the literature, and between those studies and our results, except for the noted discrepancy with the Dunne et al. (2009) SSFR–M_* relation as a result of different stellar-mass estimation routes.

7.1.2 Dependence on Redshift

Redshift evolution of SSFR (measured by n; see Figure 7) is much faster for the full sample than for the starburst sample.

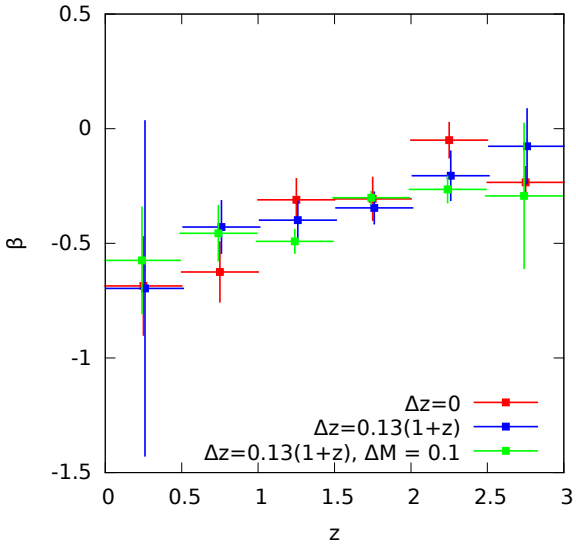

Figure 8. Mass gradient β as a function of redshift for the full sample with (blue) and without (red) the effect of photometric-redshift errors included. The green points further include a contribution from stellar-mass uncertainties. There is no discernable difference in either the values nor in the shape of $\beta(z)$.

Evolution of the irregulars is the slowest of all our samples, and for the ellipticals n is slightly steeper than for the full sample at all redshifts.

Ignoring the lowest-mass bin with its low-number statistics, the slopes for the three different populations are very different: those for the irregular and starburst samples are consistent with being independent of mass, whereas the ellipticals exhibit a negative slope ($\mathrm{d}n/\mathrm{d}M < 0$). Hence, star formation in the higher-mass ellipticals does not evolve as much as in the lower-mass ellipticals. We further find for all samples that as higher-redshift objects are included, there is some evidence that the mean level of n decreases.

Karim et al. (2011) find an increasing dependence of n_{all} on stellar mass ($\mathrm{d}n/\mathrm{d}M > 0$), though with a relatively shallow gradient. Also, their n values for the full and starburst samples are systematically higher than ours, i.e. evolution is consistently faster. Karim et al. (2011) note that at $z > 1$ their redshift-evolution parameter n_{all} is similar to the radio-luminosity redshift dependence of $(1+z)^{3.8}$. SSFR is proportional to $L_{1.4}$ (equation 3), implying that systematic errors in the median redshift estimator — and hence in their results — are limited. We do see the same in our full sample (supporting the robustness of our conclusions), but not for the irregular or starburst samples.

In conclusion, for both the full and starburst samples, we find that SSFR–redshift evolution is largely consistent between the VIDEO and COSMOS data sets, though the evolution parameter n is slightly lower in our data.

7.2 Specific Star-Formation Rates for the Henriques et al. (2012) Semi-Analytic Model

In order to relate our results to simulations, we drew a sample of galaxies from the semi-analytic model of Henriques et al. (2012) that had been overlaid on the Millennium simu-

lation (Springel et al. 2005, Guo et al. 2011). The Henriques et al. (2012) model was specifically designed for comparison with deep, high-redshift surveys such as VIDEO. Each pencil beam has an area of 1.4×1.4 square degrees and includes all the observables required: photometry from 4000 right through to $6\,\mu$m, redshifts, star-formation rates and stellar masses. Note that because of the resolution of the Henriques et al. (2012) model, the usable stellar mass is restricted to $M_* > 10^9 M_\odot$. Further, just as for the VIDEO data set, we also restricted the Henriques et al. (2012) sample to $K_\mathrm{s} < 23.5$.

Figure 9 shows SSFR as a function of mass and redshift for this simulation. Overall, SSFR amplitudes compare favourably between the Henriques et al. (2012) and VIDEO samples. It is evident that the trend of SSFR against redshift, and against mass, is roughly the same for the simulated and radio-derived SSFRs: SSFR increases with redshift but decreases with stellar mass.

This tendency for SSFR to decrease with stellar mass (Figure 9(a)), has the slope β *steepening* at higher redshift, in contradiction to our findings and those from Karim et al. (2011) (see section 7.1). The SSFRs in the Henriques et al. (2012) simulation are lower than ours and those from Karim et al. (2011), but on the other hand the Henriques et al. (2012) results are more consistent with those from UKIDSS–UDS. Figure 9(a) reveals that at low z the SSFR range is two decades in SSFR, but this reduces to about one decade at high z. For the redshift evolution of SSFR (Figure 9(b)), n is very roughly constant with stellar mass, which is consistent with our values and those of Karim et al. (2011) for all galaxies. The SSFR–M_* bimodality (see section 7.1.1) is present in the Henriques et al. (2012) simulation, but only hinted at in our data at the lowest redshifts.

Directly comparing (Figure 10) the star-formation rates from this work to those from the Henriques et al. (2012) simulation, for each mass-redshift bin, the Henriques et al. (2012) SFRs and those presented here are generally inconsistent. From Figure 10(a) we cannot tell whether the observed difference between simulated and measured SSFRs is due to discrepancies in SFRs or in stellar masses; Figure 10(b) confirms that the discrepancy could be in (at least) the SFRs, since the VIDEO SSFRs are, like the SFRs, consistently higher than those derived from the Henriques et al. (2012) simulation. Serjeant et al. (2008) stacked SCUBA and *Spitzer* data and like us compared their results to those from the Henriques et al. (2012) simulation of De Lucia et al. (2006). They also found a large discrepancy between their submm observations and the Henriques et al. (2012) simulated SSFRs. They consider several possible explanations for this inconsistency: (i) photometric redshift errors (discounted by Serjeant et al. 2008), (ii) a top-heavy initial mass function in star-forming galaxies, or (iii) that observed submm fluxes are controlled by cirrus heated by galaxies' interstellar radiation fields. In our case, either the simulation may be underestimating the SFR (as suggested by Serjeant et al. 2008), or low-level AGN activity may be contributing spuriously to the observed radio SFRs. Although it is not possible to distinguish these two scenarios without, for example, high-resolution radio imaging or X-ray data to isolate AGN cores, we argue in section 7.4 that AGN activity is not the dominant effect.

7.3 Far-Infrared Star-Formation Rate Indicators

Using *Herschel* (Poglitsch et al. 2006; Griffin et al. 2007) data from the Great Observatories Origins Deep Survey (GOODS; Dickinson et al. 2003), Elbaz et al. (2011) found evolution of SSFR with redshift for star-forming galaxies (see their Figure 18), although it is not clear to what mass range their data are sensitive. Their star-formation indicator is the so-called IR8, the ratio of the 24- and 8-μm luminosities. Stacking from 24μm into PACS-100μm leads to a measurement of evolution n of SSFR with redshift that is extremely similar to ours if we equate our full sample with their 'normal star-forming galaxies', the median SSFRs both rising from $0.1\,\mathrm{Gyr}^{-1}$ at $z = 0$ to $\approx 5\,\mathrm{Gyr}^{-1}$ by $z = 3$. As noted earlier, our starburst SSFRs fall comfortably within the zone specified by Elbaz et al. (2011), i.e., the two data sets are compatible.

Rodighiero et al. (2010) derived SSFRs directly from 24-μm *Herschel*-PACS over GOODS–N, finding instead for this star-forming sample that although SSFR does increase with redshift (for $M_* > 10^{11} M_\odot$) by a factor of about 15 from $z = 0$ to $z = 2$, it has already flattened off by $z \approx 1.5$. In their analysis for a star-forming sample, the general trend of downsizing is once again upheld; however, the dependence of SSFR on stellar mass *steepens* with redshift ($\mathrm{d}\beta/\mathrm{d}z < 0$), from a flat slope ($\beta = 0$) at $z < 1$ to $\beta = -0.50^{+0.13}_{-0.16}$ by $z \approx 2$, in broad agreement with the Dunne et al. (2009) result. This is still consistent with our (and the Karim et al. 2011) scenario in which β_{sbn} is independent of z.

SFRs were measured by Wang et al. (2013) for 3.6-μm-selected star-forming galaxies in the *Herschel* Multi-tiered Extragalactic Survey (HerMES; Oliver et al. 2012). One of the three fields studied is in fact the COSMOS field with the Karim et al. (2011) photometric redshifts and stellar masses determined using Le Phare. Rather than extrapolating the infrared luminosity L_IR (8–1000 μm) from 24-μm data, SEDs are fitted at 24 μm and to the FIR bands of 250, 350 and 500 μm where possible. L_IR in turn gives the SFR via the simple Kennicutt (1998) relation. For undetected (at SPIRE wavelength) galaxies, which make up 70 per cent of the sample, the SFR is calculated from the optical SED fit. Wang et al. (2013)'s SSFR–M_* slope β flattens slightly with redshift ($\mathrm{d}\beta/\mathrm{d}z > 0$, up to $z = 2$), but the gradient is still compatible with our measured independence of β with z.

In summary, downsizing prevails irrespective of the waveband used. A key result is that there is broad agreement between indicators (including ours) that SSFR flattens off by $z \approx 3$. Although the level of the SSFR–mass slope $\beta \approx -0.5$ is roughly consistent for star-forming samples across indicators, there is not a clear picture on its evolution with redshift $\beta(z)$, and more work is needed in this area.

7.4 AGN Contamination

AGN contamination could be a major reason to doubt that 1.4-GHz radio emission might reliably trace star formation. Dunne et al. (2009) demonstrate that there are two reasons why this is not a serious concern:

(i) First, Reddy et al. (2005) and Daddi et al. (2007) both measure contamination to SFRs from X-ray-emitting AGN, but find that contamination due to such sources decreases

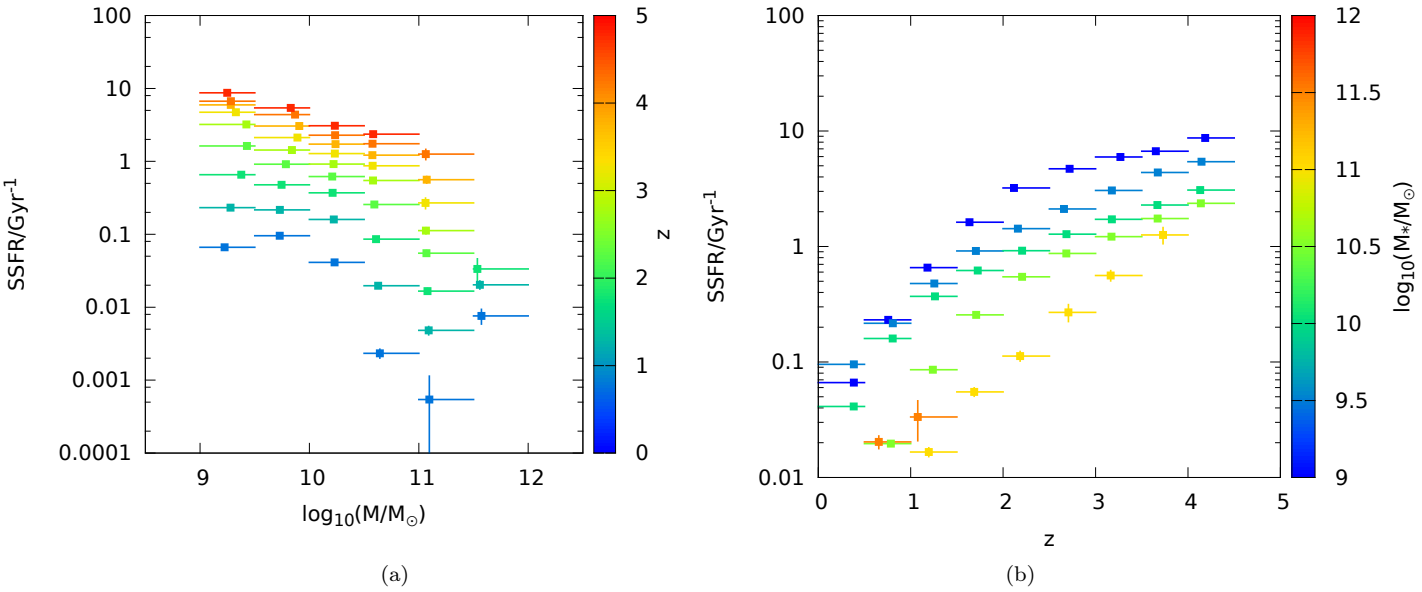

(a) (b)

Figure 9. SSFR as a function of (a) stellar mass given redshift and (b) redshift given stellar mass for all galaxies in the Henriques et al. (2012) simulations. The squares are centred on the median stellar mass in each bin. Horizontal bars indicate the width of those bins, while the vertical error bars simply reflect the poisson uncertainties. We have included the points for $3 < z < 5$ since they are available.

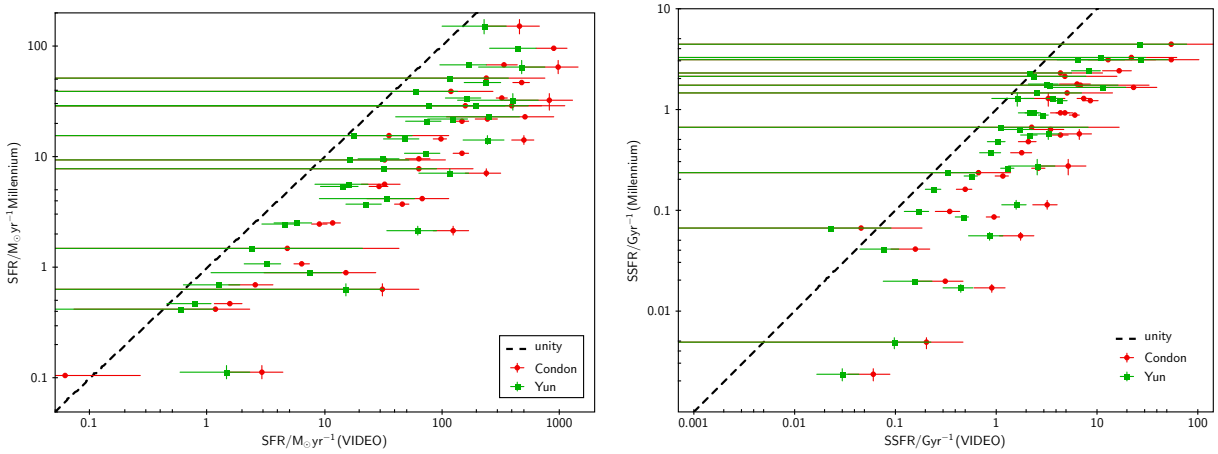

(a) (b)

Figure 10. Comparison of star-formation rates from this work and from the Henriques et al. (2012) simulation: The diagrams show median (a) SFR and (b) SSFR for each mass-redshift bin (in this case, $0 < z < 5$). In each one, the Condon et al. (2002) conversion (equation 3) is indicated with red circles while the green squares use that from Yun et al. (2001), which differs solely by a factor of two. Unity slope is marked with a black dashed line.

significantly as one moves to fainter K-band fluxes (just 3–4 per cent by K=22.9, down from up to ≈ 30 per cent at K=19.9). There is also circumstantial evidence (supported by Fomalont et al. 2006, Bondi et al. 2007 and Simpson et al. 2012) that the AGN fraction decreases significantly below 1.4-GHz fluxes of ≈ 100 μJy.

(ii) Second, radio-loud Seyfert galaxies may cause a departure from the radio-FIR correlation, but Dunne et al. (2009) demonstrate that this is not the case by comparing their radio-derived results to those from the submm.

Muxlow et al. (2005) made deep (≈ 3 μJy) 1.4-GHz VLA images of the *Hubble* Deep Field, determining that the proportion of starburst systems increases with decreasing flux right down to that level. Nearly all their faintest detections are resolved and so unlikely to be AGN. This was also predicted in the SKADS simulations of Wilman et al. (2008, 2010).

Karim et al. (2011) further found no evidence for AGN contamination in their analysis, and point out that median stacking would tolerate such contamination even if it were present. This highlights the resistance of our median-stacking results to moderate levels of AGN contamination. Pannella et al. (2009) took particular care to clean AGN from their sBzK sample; any contamination in our

VLA data would tend to flatten β, but if anything we see lower/consistent values than their already flat value of β. We therefore argue that AGN contamination is not a significant effect for our data set.

8 CONCLUSIONS

We have stacked deep (17.5 μJy) VLA radio observations at the positions of K_s-selected sources in the VIDEO field (for K_s <23.5, sensitive to $0 < z \lesssim 5$). Stellar masses and redshifts were estimated by fitting spectral templates to 10-band photometry. We separated galaxies into different populations (ellipticals, irregulars and starbursts) based on their best-fitting spectral classification. We used median single-pixel stacking, converting the stacked radio fluxes to star-formation rates using the Condon et al. (2002) relation. Specific star-formation rates, as expected, were highest for starburst galaxies and lowest for ellipticals.

(i) We subdivided the samples into stellar-mass and redshift bins, then fitted specific star-formation rates as a separable function of stellar mass and redshift in each bin. We found that SSFR falls with stellar mass for both our full and starburst samples. Hence the 'downsizing' scenario is supported by our data because we measure $\beta < 0$.

(ii) The SSFR–mass gradients β became less steep with redshift (from $\beta \approx -0.75$ to $\beta \approx -0.25$ out to $z \simeq 2$) for the full and elliptical samples, but were independent of redshift ($\beta \approx -0.5$) for the starburst and irregular galaxies.

(iii) We have compared our results to those from other radio star-formation rate indicators. We found that the evolution of the SSFR–mass slopes as a function of redshift, for both our full and starburst samples, are especially consistent with those from the COSMOS study by Karim et al. (2011), becoming less steep out to $z \simeq 2$ for the full sample. Given methodological differences, our results are also consistent with those of Dunne et al. (2009). A bimodality in the SSFR–mass plane present in the observational work of Dunne et al. (2009) and Karim et al. (2011) and in the semi-analytic models of Henriques et al. (2012) is only hinted at in our two lowest redshift bins.

(iv) We compared our results to those generated from the Henriques et al. (2012) simulation, and discovered (in all cases for our full sample) that the SSFR–mass slopes are highly inconsistent with those from our study and from Karim et al. (2011), steepening with redshift where ours both flatten out.

(v) For far-infrared indicators covering star-forming samples, the picture that emerges from the literature is not a clear one, but our result that β is independent of z lies somewhere between the extreme cases of Rodighiero et al. (2010) and Wang et al. (2013).

(vi) For the SSFR–redshift relation, we found evolution to be fastest among lower-mass ellipticals, whereas starbursts and irregulars tend to co-evolve independent of mass. The rate of evolution reduces as higher-redshift objects are included.

(vii) On the topic of AGN contamination, there is strong evidence from the literature that this would not adversely affect out results. However, we do note that high-resolution radio (e.g. from the forthcoming MeerKAT telescope, e-MERLIN or VLBI) or X-ray imaging (cf. Pannella et al. 2009) would be beneficial in resolving this issue.

ACKNOWLEDGMENTS

JZ and RD gratefully acknowledge South Africa National Research Foundation Square Kilometre Array Research Fellowships. MJ, KK and NM are grateful to the South Africa National Research Foundation Square Kilometre Array Project for financial support. We thank Russell Johnston, Mathew Smith, Matthew Prescott, Mattia Vaccari, Lingyu Wang, Bruce Bassett and Michelle Knights for useful discussions. We are thankful to the anonymous referee for their helpful comments. The project was initiated at the Cape Town International Cosmology School in January 2012, organized by AIMS, ICTP and UWC, and continued at the PARSLEY 2013 workshop of the University of the Western Cape.

REFERENCES

Arnouts S., Cristiani S., Moscardini L., Matarrese S., Lucchin F., Fontana A., Giallongo E., 1999, MNRAS, 310, 540
Baldry I. K., et al., 2010, MNRAS, 404, 86
Bauer A. E., Conselice C. J., Pérez-González P. G., Grützbauch R., Bluck A. F. L., Buitrago F., Mortlock A., 2011, MNRAS, 417, 289
Behroozi P. S., Wechsler R. H., Conroy C., 2013, ApJ, 770, 57
Bell E. F., 2003, ApJ, 586, 794
Bell E. F., et al., 2005, ApJ, 625, 23
Bondi M., Ciliegi P., Venturi T., Dallacasa D., Bardelli S., Zucca E., Athreya R. M., Gregorini L., Zanichelli A., Le Fèvre O., Contini T., Garilli B., Iovino A., Temporin S., Vergani D., 2007, A&A, 463, 519
Bondi M., et al., 2003, A&A, 403, 857
Bourne N., Dunne L., Ivison R. J., Maddox S. J., Dickinson M., Frayer D. T., 2011, MNRAS, 410, 1155
Bourne N., et al., 2012, MNRAS, 421, 3027
Bruzual G., Charlot S., 2003, MNRAS, 344, 1000
Burgarella D., et al., 2013, A&A, 554, A70
Calzetti D., 2012, preprint: astro-ph.CO/1208.2997
Cava A., et al., 2010, MNRAS, 409, L19
Chabrier G., 2003, PASP, 115, 763
Coleman G. D., Wu C.-C., Weedman D. W., 1980, ApJS, 43, 393
Condon J. J., 1992, ARA&A, 30, 575
Condon J. J., Cotton W. D., Broderick J. J., 2002, AJ, 124, 675
Condon J. J., Cotton W. D., Fomalont E. B., Kellermann K. I., Miller N., Perley R. A., Scott D., Vernstrom T., Wall J. V., 2012, ApJ, 758, 23
Cowie L. L., Songaila A., Hu E. M., Cohen J. G., 1996, AJ, 112, 839
da Cunha E., Charlot S., Dunne L., Smith D., Rowlands K., 2012, in Tuffs R. J., Popescu C. C., eds, IAU Symposium Vol. 284 of IAU Symposium, MAGPHYS: a publicly available tool to interpret observed galaxy SEDs. pp 292–296

Daddi E., Dickinson M., Morrison G., Chary R., Cimatti A., Elbaz D., Frayer D., Renzini A., Pope A., Alexander D. M., Bauer F. E., Giavalisco M., Huynh M., Kurk J., Mignoli M., 2007, ApJ, 670, 156
Daddi E., et al., 2007, ApJ, 670, 173
Damen M., Labbé I., Franx M., van Dokkum P. G., Taylor E. N., Gawiser E. J., 2009, ApJ, 690, 937
De Lucia G., Springel V., White S. D. M., Croton D., Kauffmann G., 2006, MNRAS, 366, 499
Dickinson M., Giavalisco M., GOODS Team, 2003, The Great Observatories Origins Deep Survey
Dole H., Lagache G., Puget J.-L., Caputi K. I., Fernández-Conde N., Le Floc'h E., Papovich C., Pérez-González P. G., Rieke G. H., Blaylock M., 2006, A&A, 451, 417
Domínguez Sánchez H., et al., 2012, MNRAS, 426, 330
Dunne L., Ivison R. J., Maddox S., Cirasuolo M., Mortier A. M., Foucaud S., Ibar E., Almaini O., Simpson C., McLure R., 2009, MNRAS, 394, 3
Elbaz D., Daddi E., Le Borgne D., Dickinson M., Alexander D. M., Chary R.-R., Starck J.-L., Brandt W. N., Kitzbichler M., MacDonald E., Nonino M., Popesso P., Stern D., Vanzella E., 2007, A&A, 468, 33
Elbaz D., et al., 2011, A&A, 533, A119
Ellis R. S., et al., 2013, ApJ, 763, L7
Feulner G., Goranova Y., Hopp U., Gabasch A., Bender R., Botzler C. S., Drory N., 2007, MNRAS, 378, 429
Fomalont E. B., Kellermann K. I., Cowie L. L., Capak P., Barger A. J., Partridge R. B., Windhorst R. A., Richards E. A., 2006, ApJS, 167, 103
Garn T., Alexander P., 2009, MNRAS, 394, 105
Griffin M., et al., 2007, Advances in Space Research, 40, 612
Guo Q., White S., Boylan-Kolchin M., De Lucia G., Kauffmann G., Lemson G., Li C., Springel V., Weinmann S., 2011, MNRAS, 413, 101
Haarsma D. B., Partridge R. B., Windhorst R. A., Richards E. A., 2000, ApJ, 544, 641
Heinis S., et al., 2013, MNRAS, 429, 1113
Helou G., Soifer B. T., Rowan-Robinson M., 1985, ApJ, 298, L7
Henriques B. M. B., White S. D. M., Lemson G., Thomas P. A., Guo Q., Marleau G.-D., Overzier R. A., 2012, MNRAS, 421, 2904
Hilton M., et al., 2012, MNRAS, 425, 540
Hoaglin D. C., Mosteller F., Tukey J. W., 1983, Understanding robust and exploratory data anlysis
Hopkins A. M., Beacom J. F., 2006, ApJ, 651, 142
Ilbert O., et al., 2006, A&A, 457, 841
Ilbert O., et al., 2009, ApJ, 690, 1236
Ivison R. J., et al., 2007, MNRAS, 380, 199
Jarvis M. J., et al., 2013, MNRAS, 428, 1281
Karim A., Schinnerer E., Martínez-Sansigre A., Sargent M. T., van der Wel A., Rix H.-W., Ilbert O., Smolčić V., Carilli C., Pannella M., Koekemoer A. M., Bell E. F., Salvato M., 2011, ApJ, 730, 61
Kennicutt J., et al., 1998, ApJ, 498, 181
Kennicutt R. C., Evans N. J., 2012, ARA&A, 50, 531
Kennicutt Jr. R. C., 1998, ARA&A, 36, 189
Kennicutt Jr. R. C., Kent S. M., 1983, AJ, 88, 1094
Kinney A. L., Calzetti D., Bohlin R. C., McQuade K., Storchi-Bergmann T., Schmitt H. R., 1996, ApJ, 467, 38
Komatsu E., et al., 2011, ApJS, 192, 18
Kurczynski P., Gawiser E., Huynh M., Ivison R. J., Treister E., Smail I., Blanc G. A., Cardamone C. N., Greve T. R., Schinnerer E., Urry M., van der Werf P., 2012, ApJ, 750, 117
Lapi A., et al., 2011, ApJ, 742, 24
Lawrence A., et al., 2007, MNRAS, 379, 1599
Lilly S. J., Le Fevre O., Hammer F., Crampton D., 1996, ApJ, 460, L1
Madau P., Pozzetti L., Dickinson M., 1998, ApJ, 498, 106
Magdis G. E., Elbaz D., Daddi E., Morrison G. E., Dickinson M., Rigopoulou D., Gobat R., Hwang H. S., 2010, ApJ, 714, 1740
Marsden G., et al., 2009, ApJ, 707, 1729
Martínez-Sansigre A., Rawlings S., Lacy M., Fadda D., Marleau F. R., Simpson C., Willott C. J., Jarvis M. J., 2005, Nature, 436, 666
Martínez-Sansigre A., Rawlings S., Lacy M., Fadda D., Marleau F. R., Simpson C., Willott C. J., Jarvis M. J., 2006, Astronomische Nachrichten, 327, 266
McCracken H. J., et al., 2012, A&A, 544, A156
Mitchell-Wynne K., Santos M. G., Afonso J., Jarvis M. J., 2013, MNRAS, preprint: astro-ph.IM/1306.3536
Moustakas J., Kennicutt Jr. R. C., Tremonti C. A., 2006, ApJ, 642, 775
Muxlow T. W. B., Richards A. M. S., Garrington S. T., Wilkinson P. N., Anderson B., Richards E. A., Axon D. J., Fomalont E. B., Kellermann K. I., Partridge R. B., Windhorst R. A., 2005, MNRAS, 358, 1159
Norman C., et al., 2004, ApJ, 607, 721
Oliver S., et al., 2010, MNRAS, 405, 2279
Oliver S. J., et al., 2012, MNRAS, 424, 1614
Pannella M., et al., 2009, ApJ, 698, L116
Papovich C., Rudnick G., Le Floc'h E., van Dokkum P. G., Rieke G. H., Taylor E. N., Armus L., Gawiser E., Huang J., Marcillac D., Franx M., 2007, ApJ, 668, 45
Pérez-González P. G., Rieke G. H., Villar V., Barro G., Blaylock M., Egami E., Gallego J., Gil de Paz A., Pascual S., Zamorano J., Donley J. L., 2008, ApJ, 675, 234
Poglitsch A., et al., 2006, in Society of Photo-Optical Instrumentation Engineers (SPIE) Conference Series Vol. 6265 of Society of Photo-Optical Instrumentation Engineers (SPIE) Conference Series, The photodetector array camera and spectrometer (PACS) for the Herschel Space Observatory
Polletta M., et al., 2008, A&A, 492, 81
Reddy N. A., et al., 2005, ApJ, 633, 748
Rodighiero G., et al., 2010, A&A, 518, L25
Roseboom I. G., et al., 2012, MNRAS, 426, 1782
Roseboom I. G., Lawrence A., Elvis M., Petty S., Shen Y., Hao H., 2013, MNRAS, 429, 1494
Schiminovich D., et al., 2007, ApJS, 173, 315
Serjeant S., et al., 2004, ApJS, 154, 118
Serjeant S., et al., 2008, MNRAS, 386, 1907
Simpson C., Rawlings S., Ivison R., Akiyama M., Almaini O., Bradshaw E., Chapman S., Chuter R., Croom S., Dunlop J., Foucaud S., Hartley W., 2012, MNRAS, 421, 3060
Smith D. J. B., et al., 2012, MNRAS, 427, 703
Springel V., White S. D. M., Jenkins A., Frenk C. S., Yoshida N., Gao L., Navarro J., Thacker R., Croton D., Helly J., Peacock J. A., Cole S., Thomas P., Couchman H., Evrard A., Colberg J., Pearce F., 2005, Nature, 435, 629

Steidel C. C., Adelberger K. L., Giavalisco M., Dickinson M., Pettini M., 1999, ApJ, 519, 1
Takagi T., Mortier A. M. J., Shimasaku K., Coppin K., Pope A., Ivison R. J., Hanami H., Serjeant S., Dunlop J. S., 2007, in Combes F., Palous J., eds, IAU Symposium Vol. 235 of IAU Symposium, Sub-millimetre properties of massive star-forming galaxies at z ˜ 2 in SHADES/SXDF. pp 429–429
Viero M. P., et al., 2013, ArXiv e-prints
Wang L., et al., 2013, MNRAS, 431, 648
White R. L., Helfand D. J., Becker R. H., Glikman E., de Vries W., 2007, ApJ, 654, 99
Wilman R. J., et al., 2008, MNRAS, 388, 1335
Wilman R. J., Jarvis M. J., Mauch T., Rawlings S., Hickey S., 2010, MNRAS, 405, 447
Wilson G., Cowie L. L., Barger A. J., Burke D. J., 2002, AJ, 124, 1258
Yun M. S., Reddy N. A., Condon J. J., 2001, ApJ, 554, 803
Zheng X. Z., Bell E. F., Papovich C., Wolf C., Meisenheimer K., Rix H.-W., Rieke G. H., Somerville R., 2007, ApJ, 661, L41
Zinn P.-C., Blex S., Seymour N., Bomans D. J., 2012, A&A, 547, A50

This paper has been typeset from a TEX/ LATEX file prepared by the author.